nature communications

Article

https://doi.org/10.1038/s41467-025-61317-9

3D ultra-broadband optically dispersive microregions in lithium niobate

Received: 21 November 2024

Accepted: 16 June 2025

Published online: 02 July 2025

Check for updates

Bo Zhang[1,7] ✉, Zhuo Wang[1,7], Tom Albrow-Owen[2,7], Tawfique Hasan[3], Zesheng Chen[3], Zhiying Song[3], Gongyuan Zhang[4], Hannah Joyce[2], Dezhi Tan[1,5] ✉, Qiangbing Guo[1], Cheng-wei Qiu[6] ✉, Zongyin Yang[1,4] ✉ & Jianrong Qiu[1] ✉

3D in-substrate integration of optical functionalities fully utilizes the vertical dimension of space and is valuable for advancing next-generation integrated optoelectronics. However, as a key optical effect, optical dispersion remains unavailable to be tailored at the microscale in 3D. We introduce artificial dispersive microregions in lithium niobate crystals to engineer free-space ultra-broadband optical dispersion. The microregions are formed by ultrafast laser-induced sub-wavelength phase-transition nanostripes, which modulate the crystal's birefringence to establish localized frequency-dependent interference of ordinary and extraordinary light. This approach operates across an ultra-broad wavelength range (>1300 nm) within an exceptionally compact volume ($50 \times 10 \times 6\ \mu m^3$), and allows for precise, on-demand dispersion control in 3D space. The dispersive microregions exhibit viewing-angle independence, stability to harsh conditions (600 °C high temperature, contamination, corrosion, and mechanical damage), and wide applicability across various birefringent crystals. We demonstrate the versatility of our method in developing broadband on-chip micro-spectrometers and applications of spectral imaging, information recording, and encryption.

Most famously exemplified by the generation of rainbows, optical dispersion is a fundamental phenomenon in physics that allows for the separation of light into its constituent spectral colors or frequencies. It plays a pivotal role in a wide range of modern applications, from scientific research to engineering technology, such as spectroscopy, advanced imaging, precise measuring, information processing, and lasers[1–8]. The recent surge in the development of on-chip, wearable, and portable optoelectronic systems has led to a rapidly growing demand for photonic integration solutions[9–12], with the next generation of devices generally demanding feature sizes toward micrometer scales. However, widely used dispersive components, such as prisms and diffraction gratings, typically require long optical path lengths, precise geometric/angular alignment, or multiple elements functioning in parallel to ensure accuracy and operating bandwidth, which is incompatible with future ultra-compact or portable designs.

Advancements in nanophotonics and material science continue to push the boundaries of what is possible. A variety of technical routes have been proposed to achieve compact dispersion footprints, including photonic crystals[13,14], waveguides[15,16], filters[17,18], photodetectors[19,20], and metasurfaces[21,22]. Despite their impressive miniaturization capabilities, these approaches still present several challenges, stemming from material stability, coupling effects, frequency-specific design, angular sensitivity, and fabrication complexity/high cost. Moreover, none of these existing miniaturized dispersion

[1]State Key Laboratory of Extreme Photonics and Instrumentation, College of Optical Science and Engineering, Zhejiang University, Hangzhou 310027, China. [2]Department of Engineering, University of Cambridge, Cambridge CB3 0FA, UK. [3]Cambridge Graphene Centre, University of Cambridge, Cambridge CB3 0FA, UK. [4]College of Information Science and Electronic Engineering, Zhejiang University, Hangzhou 310027, China. [5]School of Material Science and Engineering, Zhejiang University, Hangzhou 310027, China. [6]Department of Electrical and Computer Engineering, National University of Singapore, Singapore 117583, Singapore. [7]These authors contributed equally: Bo Zhang, Zhuo Wang, Tom Albrow-Owen. ✉e-mail: zhangbobo@zju.edu.cn; wctdz@zju.edu.cn; chengwei.qiu@nus.edu.sg; yangzongyin@zju.edu.cn; qjr@zju.edu.cn

technologies offer 3D integrability, which is crucial for maximizing the spatial efficiency and flexibility of modular optical elements. Hence, there remains a need to establish a general micrometer-scale optical dispersion (MOD) platform that combines broadband operation, high robustness, production simplicity, and controllability in 3D space.

Lithium niobate ($LiNbO_3$) is a versatile substrate material for advancing optoelectronic technologies due to its excellent physicochemical properties and machinability[23–27]. Recent studies have demonstrated the inscription of functional structures such as optical waveguides[28–30], nonlinear photonic crystals[31,32], and poled ferroelectric domains[33,34], within $LiNbO_3$ crystals for 3D photonic applications. With an ultra-broad transparency window, excellent stability, and pronounced optical dispersion, $LiNbO_3$ crystal offers an ideal platform for 3D integration of high-performance MOD functionalities. However, it remains a great challenge to determine and control the microscopic light dispersion behaviors in the $LiNbO_3$ crystal matrix due to the absence of a dispersive structure that can effectively function in the high-refractive-index dielectric environment.

This article presents previously unrealized 3D optically dispersive microregions in $LiNbO_3$ crystals, formed by ultrafast laser-induced sub-wavelength phase-transition nanostripes (SPNs). These microregions modulate the crystal's intrinsic birefringence to achieve microscopic control of optical dispersion with multiple degrees of freedom in 3D space. Through this method, it is possible to produce MOD elements that can modulate light over an ultra-broad wavelength range, in principle limited only by the transparency window of the matrix, and can be widely extended to other birefringent crystals. The dispersive microregions also have no angular dependence and can function in both transmission and reflection modes, allowing for straightforward integration with various optical devices. All of these factors give this approach significant advantages for miniaturized spectrally sensitive applications. As a proof of concept, we produce an on-chip micro-spectrometer with a broadband operational range (390–1710 nm) and notable spectral resolution (~4 nm). Furthermore, we also demonstrate spectral imaging, chromatic information recording, and optical encryption applications to showcase the potential of this versatile platform for broadband, robust, and miniaturized integrated optoelectronic technologies.

Results

Dispersive microregion and MOD generation in $LiNbO_3$ crystal

Figure 1 illustrates the creation and functionality of dispersive microregions within a single-crystalline $LiNbO_3$ sample. As shown in Fig. 1a, ultrafast laser-induced self-organized nanostructuring is applied to produce SPNs. During ultrafast laser irradiation in transparent dielectrics, plenty of nanoplasmas can be excited, and their anisotropic growth driven by local field enhancement leads to nanoscale periodic material modifications within the focal volume[35,36]. This self-organization process is straightforward and efficient, enabling high-throughput patterning of regularly arranged periodic nanostructures in transparent dielectric crystals[37,38]. Under our experimental conditions, amorphous nanostripes of width ~20 nm are inscribed in the $LiNbO_3$ crystal matrix at a periodicity of ~200 nm (Fig. 1b and Supplementary Fig. 2). The refractive index difference between the amorphous phase and the crystalline phase of $LiNbO_3$ is as large as 0.3[39]. According to effective medium theory[40], the SPNs can be regarded as an artificial anisotropic medium for modulating light propagating in the crystal (Supplementary Note 1), which is confirmed by the quantitative birefringence imaging and polarization-dependent transmission tests of the laser-modified zone (Supplementary Fig. 3).

Owing to the intrinsic birefringence effect of $LiNbO_3$ crystal, the incident polychromatic light will be split into ordinary (O) and extraordinary (E) light beams. The MOD is essentially the frequency-dependent interference of O and E light. In this study, the dispersive microregion with SPNs does not directly disperse light like a traditional diffraction grating but functions as an integrated assembly of a waveplate and a polarizer to locally modulate O and E light (Fig. 1c), making them interfere within an ultra-compact footprint (Fig. 1d). The Jones matrix of this MOD element can be written as follows:

$$G = \begin{bmatrix} cos^2\beta & \frac{1}{2}sin2\beta \\ \frac{1}{2}sin2\beta & sin^2\beta \end{bmatrix} \begin{bmatrix} 1 & 0 \\ 0 & e^{i\varphi} \end{bmatrix} \quad (1)$$

where G is the Jones matrix of the dispersive microregion; β is the angle between the transmission axis of SPNs and the Y-axis; φ is the phase difference between O and E light.

The original dispersion comes from the frequency-dependent phase difference of O and E light when propagating in the $LiNbO_3$ crystal. When the O and E light reach the dispersive microregion, their phase difference (φ) can be described as:

$$\varphi = \frac{2\pi d}{\lambda}\left|n_o - n_e\right| \quad (2)$$

where λ is the incident light wavelength; d is the distance that O and E light travels before reaching the dispersive microregion; n_o and n_e are refractive indices of O and E light, respectively. As the refractive index is a function of wavelength (Supplementary Fig. 4a), the induced phase difference depends on the wavelength (λ) and the distance (d). When d is a fixed value, only O and E light of a specific wavelength can interfere in the dispersive microregion, resulting in monochromatic interference. In this condition, monochromatic MOD signals can be observed (Fig. 1e). To establish broadband interference, a wedge angle (θ) is introduced to create a continuous variation in d along the writing path, in turn resulting in a continuously varying phase difference (Supplementary Fig. 4b). In this way, simply by engineering the laser writing path to construct the wedge angle, O and E light can be modulated to interfere across all illumination wavelengths, with the interference patterns of different wavelengths orderly arranged within the dispersive microregion, resulting in the generation of chromatic MOD signals (Fig. 1f).

In summary, this strategy enables 3D direct writing of microscale dispersive microregions in a single step within a standard optical crystal, representing a significant advantage over conventional fabrication technologies for dispersive elements. The dispersive microregion functions like an interferometer embedded inside the crystal matrix, allowing the frequency-dependent phase difference between O and E light to manifest as an interference signal within it, which allows for straightforward MOD detection. In contrast, dispersion signals induced by gratings, prisms, or beam splitters are emanative and weak at the micrometer scale (Supplementary Fig. 5) and cannot be effectively tailored or collected.

On-demand MOD control in 3D space

Tailoring the writing design of the dispersive microregion allows for highly controllable MOD characteristics. Typically, the lithography is performed with the laser incident along the optical axis (i.e., vertical writing), which allows for the rapid generation of a highly regular dispersive microregion, as well as reducing its working thickness, thereby minimizing optical loss. In this writing mode, the spectrophotometric direction can be finely adjusted by twisting the dispersive microregion in 3D space. This can be achieved by introducing double wedge angles (θ and α) (Fig. 2a). The presence of two wedge angles leads to the simultaneous arrangement of the interference fringes of O and E light in two directions, resulting in specific spectral distribution characteristics in the dispersive microregion (Fig. 2b). As the wedge angle determines the phase difference gradient of O and E light on reaching the dispersive microregion, tuning the wedge angle value allows for manipulation of the interference fringes of light with

https://doi.org/10.1038/s41467-025-61317-9

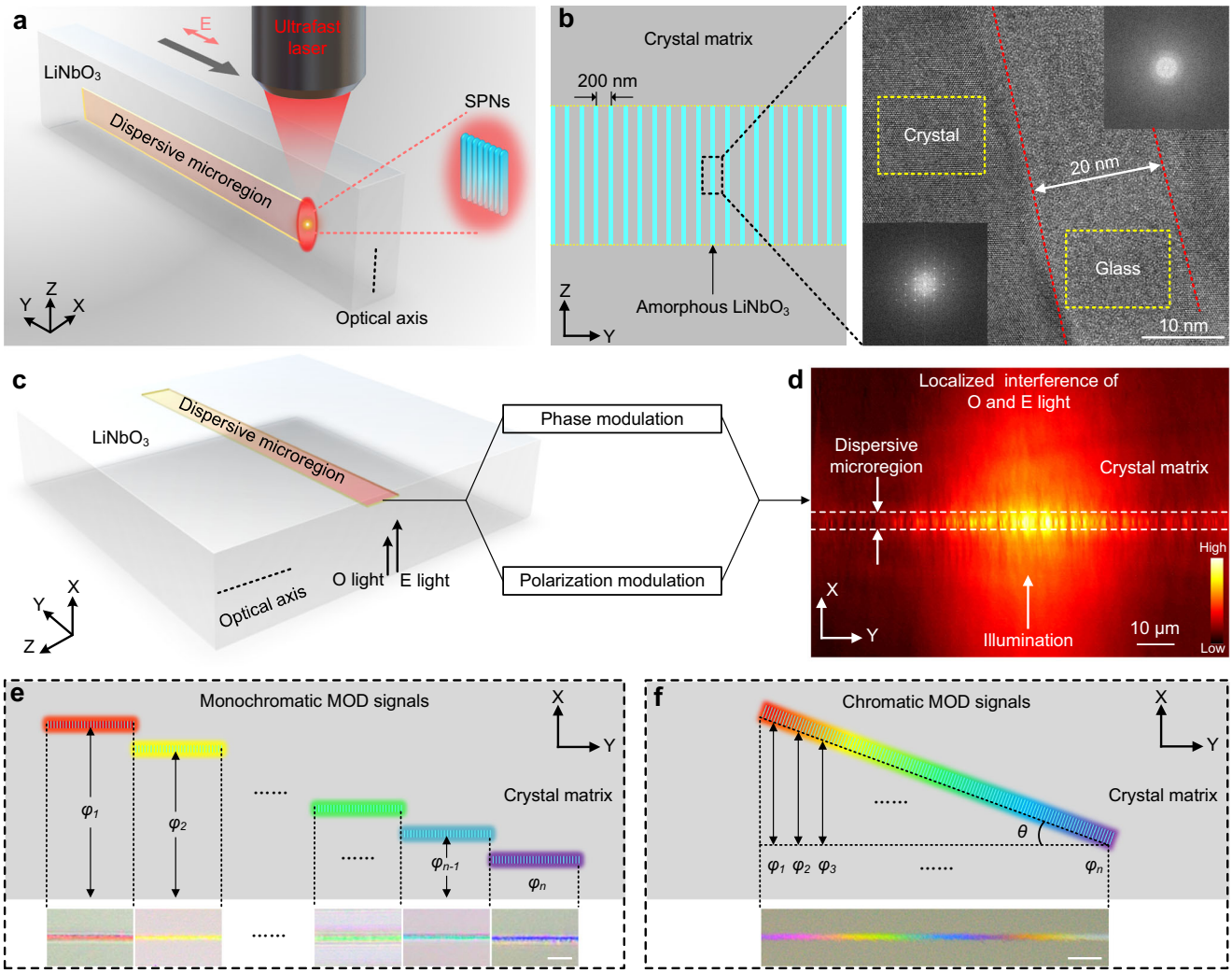

Fig. 1 | Mechanism of MOD. a Schematic of dispersive microregion creation in the $LiNbO_3$ crystal matrix. Black arrow indicates the writing direction. E indicates the laser polarization. **b** Schematic of the inner structure of a dispersive microregion (left) and high-resolution transmission electron microscope (HRTEM) image of crystal-to-amorphous phase transition zone (right). Insets: fast Fourier transform (FFT) images of the dotted areas. **c** Schematic of the optical modulations offered by SPNs in the dispersive microregion. **d** Experimentally observed localized interference of O and E light in the dispersive microregion. Color bar: light intensity. **e** Schematic of generating monochromatic MOD signals with dispersive microregions (up) and experimental results (down). Scale bar: 10 μm. **f** Schematic of generating chromatic MOD signals with an angled dispersive microregion (up) and experimental result (down). Scale bar: 50 μm. φ_n indicates the phase difference of O and E light induced by different optical paths.

different wavelengths, which can be described as:

$$e = \frac{\lambda}{\theta |n_o - n_e|} \tag{3}$$

where e is the interval of interference fringes, λ is the wavelength of O and E light, θ is the wedge angle, n_o and n_e are refractive indices of O and E light. Theoretically, the larger the wedge angle, the smaller the interval of interference fringes of different wavelengths (Fig. 2c), leading to a denser packing of these fringes within the dispersive microregion (Fig. 2d). Therefore, adjusting the wedge angle allows for direct control over the spectrophotometric length of MOD, that is, the minimum length of the dispersive microregion required for separating light with different wavelengths in a specific waveband. For instance, in the visible waveband (400–780 nm), increasing the wedge angle to more than 5° can reduce the spectrophotometric length to less than 70 μm (Fig. 2e).

In addition, the substantial refractive index contrast between O and E light in the $LiNbO_3$ crystal facilitates the more efficient generation of gradient phase differences, enabling the optical wedge to operate on the micrometer scale (Supplementary Note 2). For example, a tiny wedge structure with a wedge angle (θ) of 6.8°, a wedge thickness (X-axis size) of ~6 μm, and a spectrophotometric length (Y-axis size) of ~50 μm can generate the dispersion covering the whole visible band (Fig. 2f). By tuning laser parameters, the minimum width (Z-axis size) of the dispersive microregion can reach ~10 μm (Supplementary Fig. 6). Thus, a volume measuring only 50 × 50 × 50 μm^3 is sufficient to accommodate several such MOD elements. The ultra-compact 3D sizes of the optical wedge allow it to be easily written into various forms of substrates, including miniaturized blocks, sheets, and even films (Supplementary Fig. 7). Apart from tuning the laser writing process, the spectral characteristics of MOD can also be manipulated via the interference modes of O and E light, namely, either constructive or destructive interference (Supplementary Fig. 8). In constructive interference mode, light at specific frequencies is enhanced, resulting in the MOD signal displaying spatially arranged color fringes that correspond to these enhanced frequencies. Conversely, in destructive interference mode, light at certain frequencies is suppressed, causing the MOD signal to exhibit complementary colors of these frequencies. By adjusting the polarization of the illuminating light, it is possible to

https://doi.org/10.1038/s41467-025-61317-9

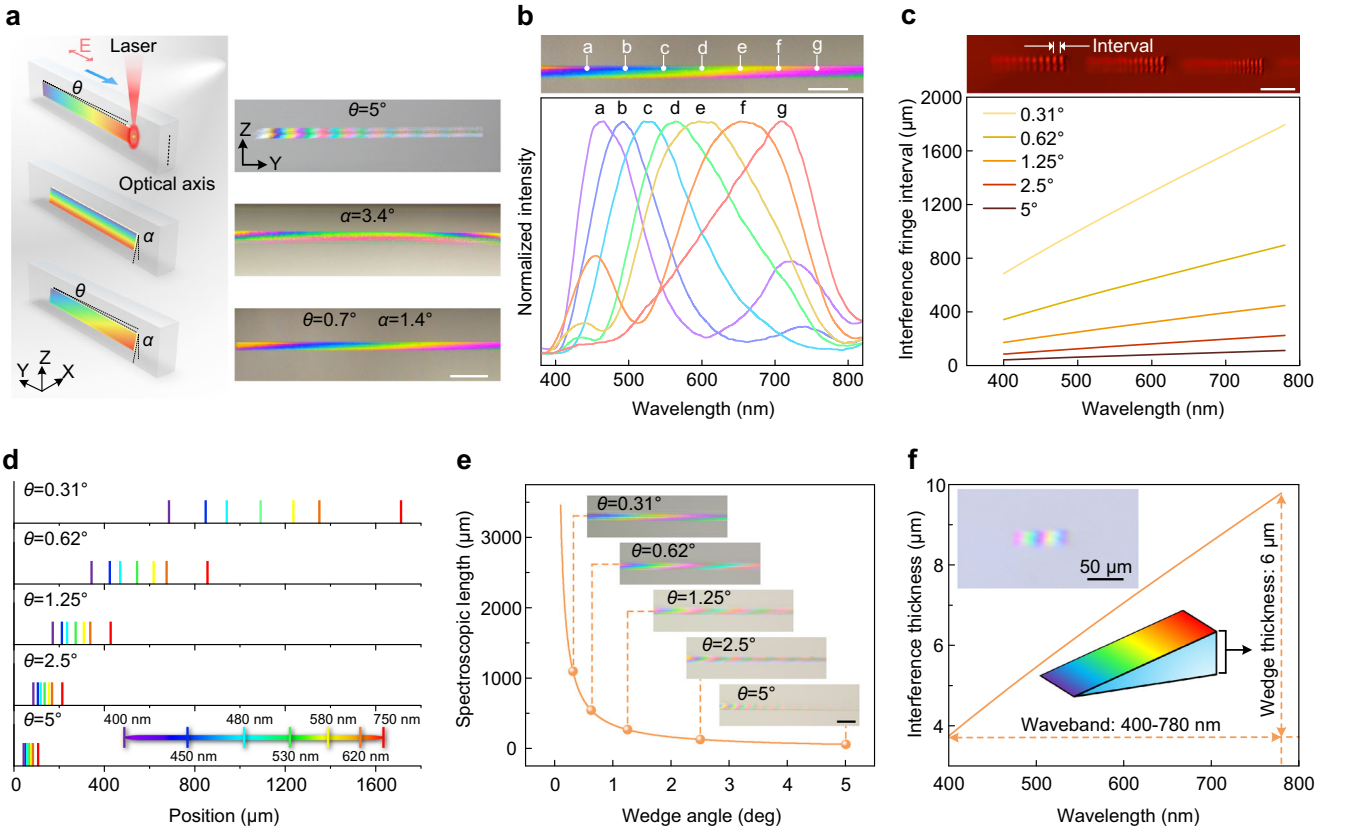

Fig. 2 | Manipulation of MOD. a Manipulation of the spectrophotometric direction of MOD signals in the crystal matrix. θ and α indicate wedge angles applied for rotating dispersive microregions in 3D space. Blue arrow indicates the writing direction. E indicates the laser polarization. Scale bar: 200 μm. **b** Spectral characterization of a dispersive microregion. Inset: representative spectrum test points in the dispersive microregion. Scale bar: 100 μm. **c** Interval of interference fringes as a function of wavelength under different wedge angles. Inset: experimentally imaged interference fringes by using 590 nm illumination. Scale bar: 100 μm. **d** Relative positions of the interference fringes of different wavelengths along the laser scanning direction. Colored lines represent the interference fringes of several representative wavelengths. **e** Spectrophotometric length as a function of the wedge angle. Insets: experimental results obtained by using corresponding wedge angles on the theoretical curve. Scale bar: 100 μm. **f** Wedge thickness as a function of wavelength. Insets: experimentally generated ultra-compact MOD (top-left) and schematic of a dispersive microregion (middle).

switch freely between these two interference modes, thereby enriching the spectral characteristics of the MOD. These results demonstrate that the MOD can be manipulated in multiple ways, providing a solid foundation for the on-demand design of MOD-based micro-nano-photonic devices.

Flexibility, adaptability, and universality of MOD strategy

The MOD approach proposed in this work combines favorable performances of both $LiNbO_3$ crystals and laser-induced SPNs. This unique dispersion mechanism offers a series of notable advantages. Firstly, the dispersion signal of MOD comes from the wedge structure, whose superiority lies in its capability to generate a continuous and broadband optical dispersion. Thus, our MOD elements show a spatially dependent spectral response that continuously varies across an ultra-wide frequency range encompassing the ultraviolet, visible, and near-infrared regions (Supplementary Movie 1), theoretically limited only by the transparency window of the $LiNbO_3$ crystal (370–5000 nm). Secondly, since detectable dispersion signals are only generated in the dispersive microregion, the shape of MOD can be easily customized by tuning the laser writing path (Supplementary Fig. 9). For more complex MOD patterning, the laser incidence is typically set perpendicular to the optical axis (horizontal writing) (Fig. 3a). In this writing mode, programming the writing path and depth along with the wedge angle enables the creation of any desired MOD patterns in 3D space, which is unique among current optical dispersion approaches. Here, we demonstrate the direct lithography of multiple highly customized monochromatic and multi-color MOD patterns (Fig. 3b), rendering our strategy promising in fields such as chromatic information recording, optical encryption, and anti-counterfeiting (Supplementary Fig. 10). Thirdly, the transparency of $LiNbO_3$ and the interference-based dispersion mechanism make the MOD signals detectable in both transmission and reflection modes with highly consistent spectral properties (Fig. 3c), which allows our MOD principle to integrate more flexibly with different types of optical systems. Additionally, the localized optical modulation induced by SPNs enables the MOD signal to be tightly confined within the dispersive microregion rather than spatially divergent. Thus, the acquisition of the MOD signal only requires imaging the SPN area and is completely independent of the viewing angle (Fig. 3d), making it highly favorable for straightforward integration of MOD elements with chip-based optical devices.

For recent advances in miniaturized spectral sensing, the presented spectral response elements or materials are often fragile and susceptible to external environments, necessitating additional protection and packaging (Supplementary Note 3). Here, encapsulated within the all-inorganic crystal matrix, MOD elements possess notable stability in various harsh environments, including high temperatures, corrosion, contamination, mechanical damage, and light damage (Fig. 3e and Supplementary Fig. 11). This positions MOD elements as an ideal choice for applications that require stringent durability, particularly in air-, water-, and space-borne missions. Significantly, ultrafast laser-induced self-organization is a widely applicable material

https://doi.org/10.1038/s41467-025-61317-9

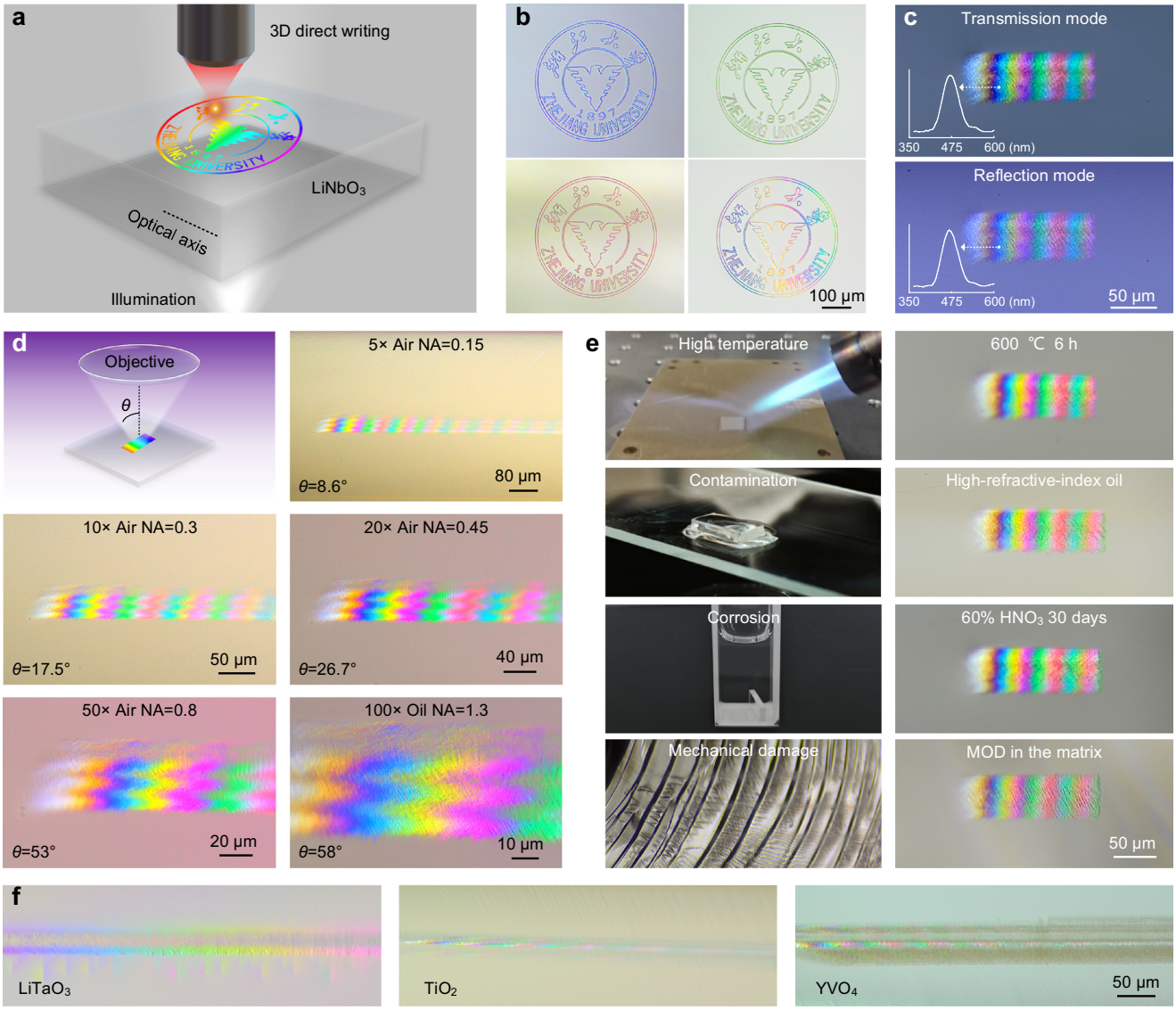

Fig. 3 | Advantageous properties of MOD. a Schematic of MOD patterning with laser incidence oriented perpendicularly to the optical axis of $LiNbO_3$. **b** Monochromatic and multi-color butterfly patterns produced by using MOD patterning. **c** MOD signals obtained in transmission mode and reflection mode. Insets: spectral properties of the marked points in the dispersive microregion. **d** Viewing angle independence of MOD verified by characterizing MOD signals under different magnifications. **e** Stability of MOD elements under harsh conditions, including high temperature, contamination, corrosion, and mechanical damage. For experimental conditions and stability assessments, see methods. **f** Universality of the MOD approach in different birefringent crystals.

modification process[41,42]. The principles proposed in this study represent a highly general methodology for engineering MOD in many birefringent crystals, rather than a unique case specific to $LiNbO_3$. As a verification, we experimentally demonstrated the generation of MOD in several significant crystalline optical media, such as lithium tantalate, titanium dioxide, and yttrium vanadate crystals (Fig. 3f). Compared to other dielectric materials, $LiNbO_3$ does present particular advantages for enhancing the optical modulation capability of the SPNs. First, $LiNbO_3$ has a large dispersion effect (i.e., more highly wavelength-dependent refractive index) and there is a substantial refractive index difference between the amorphous and crystalline phases of $LiNbO_3$ (~0.3), ensuring the optical modulation capacity of SPNs. More importantly, the O and E light in $LiNbO_3$ has a large refractive index contrast, facilitating the generation of substantial phase differences, even with short optical path lengths. In contrast, although lithium tantalate also enables the generation of MOD, its signals are much weaker than those produced by $LiNbO_3$ due to the small refractive index difference between its O and E light (Supplementary Fig. 12). In addition, $LiNbO_3$ has excellent machinability and is adapted to precision cutting, polishing, and filming, which allows us to integrate MOD functionalities into various types of substrates. In contrast, the machining of many crystals (e.g., aluminum oxide) remains a great challenge due to their high hardness. While at this stage $LiNbO_3$ emerges as the matrix material with the most favorable overall performance, future discoveries may yield even superior matrix materials.

These significant advantages allow MOD elements to be widely adapted to diverse substrates, working conditions, and commercially mature devices, providing expandable and robust dispersion functions for novel integrated optical systems.

Spectroscopic applications of MOD components

As a proof of concept, we explore the significant potential of our MOD strategy by demonstrating its application in on-chip integrated spectrometers. Here, a $LiNbO_3$ sheet written with the dispersive microregion is bonded with at least one polarizing film to form a

functionalized window that can be directly coupled to an image sensor (Fig. 4a). As the MOD function can only be activated in chromatic polarization mode, the MOD signals can be generated and eliminated on demand according to specific application scenarios (Supplementary Fig. 13). The all-dielectric dispersive microregion has little effect (transmittance reduced by less than 10%) on the device's imaging function (Supplementary Fig. 14). In chromatic polarization mode, MOD signals can be efficiently captured as pixelated images by the image sensor. The exposure time required is generally less than 100 ms. To realize spectroscopic functions, the spectrometer is first calibrated by measuring the spectral response of the MOD element: the spatial intensity distribution as a function of the illumination wavelengths in the dispersive microregion (Fig. 4b). Then, the spatial intensity distribution patterns of the unknown incident light are captured, and the spectral information can be reconstructed by processing the obtained response functions together with captured MOD image data under illumination by a sample of unknown light sources. During the reconstruction process, an adaptive Tikhonov regularization strategy is applied to increase reconstruction accuracy (Supplementary Note 4).

As demonstrated in Fig. 4c, the MOD spectrometer exhibits a sensitive, continuous, and consistent spectral detection capability over an ultra-broad operating wavelength range, spanning the entire visible and short-wavelength infrared regions from ~390 nm to ~1710 nm. To more intuitively demonstrate the operation of our device in a real-world setting, we have further provided a video showing its real-time spectral information output capability for unknown light sources of varying wavelengths (Supplementary Movie 2). The working waveband of the MOD spectrometer shown here is limited by the spectral response range of the available image sensor in our

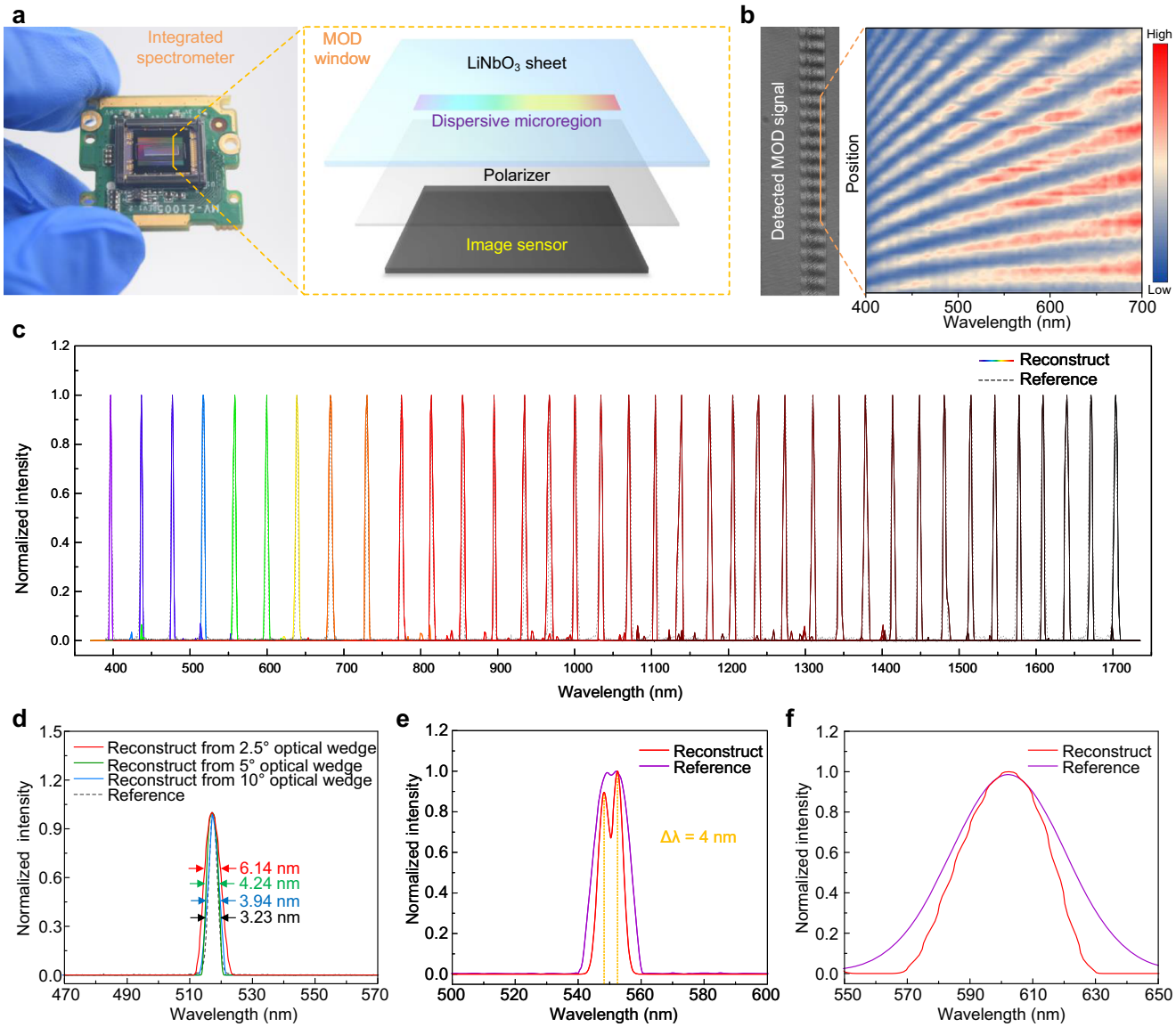

Fig. 4 | Spectrum detection through MOD. a Typical usage of a MOD window in an integrated spectrometer design. An experimentally produced MOD spectrometer (left) and a schematic diagram of its functional framework (right). **b** Detected MOD signal under the illumination of monochromatic light source (left) and spectral response matrix of the MOD element (right). Color bar: light intensity. **c** Spectra of a range of separate monochromatic light signals at 37 different wavelengths across the visible to near-infrared range (390–1710 nm), as measured by our reconstructive spectrometer (colored lines) and reference commercial spectrometers (black dotted lines). **d** Reconstruction accuracy optimization by adjusting the wedge angle. Illumination monochromatic light is centered at 517 nm. Arrows indicate FWHM. **e** Reconstruction of two mixed narrow-band signals with peaks separated by 4 nm. **f** Reconstruction of a continuous broadband spectrum. Reference spectra are measured using a commercial spectrometer.

laboratory. Therefore, although our MOD element could exhibit spectral responses over an ultra-wide spectral range in the transparency window of the $LiNbO_3$ crystal, it is necessary to properly select the image sensor for integration to capture the MOD signal according to the specific application scenario, such as choosing between a visible light-sensitive image sensor or an infrared light-sensitive image sensor.

More importantly, the detection accuracy and spectral resolution of the MOD spectrometer can be further optimized by adjusting the wedge angle. Here, we demonstrated the light reconstruction capability of MOD elements with varying wedge angles from 2.5° to 10°. The reconstruction accuracy shows a clear improvement as the wedge angle increases. The full width at half maximum (FWHM) of reconstructed monochromatic light can reach 3.94 nm when using a 10° wedge angle, almost equal to that of the reference spectrum (3.23 nm) measured by commercial spectrometers (Fig. 4d). This improvement arises from the fact that increasing the wedge angle results in a reduction in the interval of interference fringes with different frequencies, making them more closely arranged in the dispersive microregion, which consequently becomes more sensitive to variations in the spectral characteristics of the incident light. After optimization, we confirmed that the MOD spectrometer can distinguish two peaks around 550 nm separated by ~4 nm (Fig. 4e). Continuous broadband spectra can also be well reconstructed with the MOD spectrometer (Fig. 4f).

Since the MOD signal is essentially a frequency-dependent interference signal, as long as there are interference fringes in the dispersive microregion, the unknown spectrum can be measured through the spectral reconstruction process. In principle, the MOD spectrometer is more suitable for analyzing unpolarized natural light. Nevertheless, we also demonstrated the capacity of our device to analyze unknown linearly polarized light sources. Our experiments indicate that even when the incident polarization deviates significantly from the optimal direction (45° to the optical axis), the reconstructed spectra still maintain fairly high accuracy in terms of the full width at half maximum difference (<1.2 nm) and peak wavelength difference (<0.3 nm) versus the reference measurement (Supplementary Fig. 17). This is because the variation of input polarization only influences the relative intensity of MOD signals rather than the structural properties of interference fringes. These results show that the MOD-based spectrometer can also be well-performed in analyzing linearly polarized incident light.

Our MOD strategy can benefit from the facile fabrication of multilayer dispersive microregions via laser direct writing to construct dispersive arrays along the Z-axis (optical axis) for spectral imaging (Fig. 5a–c). We demonstrate spectral imaging of a color filter consisting of blue, green, and red areas using our MOD spectrometer (Fig. 5d). During the imaging process, the interference patterns of dispersive microregions in the dispersive array are captured and converted to spectral data (Fig. 5e). The pixel resolution of our spectrometer depends on both the image sensor used and data processing during spectral reconstruction. At the current stage, the pixel resolution of our spectrometer theoretically reaches approximately 768 × 512 (Supplementary Note 4 and Supplementary Fig. 18), comparable to current proof-of-concept and commercially available devices[43,44], which can be further enhanced by using image sensors with higher pixel resolutions. An advantage of this configuration is its ability to acquire both geometric and spectroscopic information simultaneously in a single capture without requiring any scanning elements or moving parts, highlighting the potential of MOD elements in hyperspectral technologies. Since SPNs are an all-dielectric structure, the dispersive microregion inherently has the advantage of low optical loss, which allows the MOD signals to be captured by the image sensor at high efficiency. The exposure time is generally less than ~100 ms, comparable to that of commercial devices[45]. After acquiring raw images, our device takes ~500 ms to reconstruct spectra. In the future, the overall response speed of the spectrometer can be further improved by optimizing the data processing algorithm. In addition, the spectroscopic device demonstrated here is fabricated using commercially available materials, elements, and simple one-step processing, with the core components costing less than $10. Given the excellent expansibility, robustness, and economic efficiency of MOD elements, such integrated spectrometers could find applications in a variety of scenarios, including environmental monitoring, biomedical, food safety, and industrial inspection, particularly in disposable/consumable mission operations under extreme conditions.

Discussion

In this study, we utilize ultrafast laser-induced SPNs as a tool to construct dispersive microregions within $LiNbO_3$ crystals. This approach, combined with polarization optics, enables localized modulation of the intrinsic birefringence of $LiNbO_3$, which can be applied to achieve the generation and manipulation of MOD in the all-inorganic crystal matrix as well as MOD-based spectroscopic applications. Compared with current methods, our dispersive components demonstrate significant advantages in several key performance indicators (Supplementary Table 1), such as environmental stability, operational bandwidth, manufacturability, and application cost. Our MOD technique is widely applicable to a variety of birefringent crystals and substrates and can be extended through multiple strategies, including further optimization of the laser writing process or harnessing superior properties of the matrix material. Indeed, $LiNbO_3$ exhibits rich nonlinear optical properties, such as electro-optical effects, acousto-optical effects, and photorefractive effects. These properties could be used to adjust the refractive index contrast between the crystalline and amorphous phases in SPNs, enabling dynamic phase modulation over O and E light and active tuning of the MOD signals. This real-time regulation of MOD would be beneficial for integrated, reconstructive spectroscopic applications because it enables an increased sampling of spectral response characteristics without increasing the number or size of dispersive microregions, potentially paving the way for higher-resolution spectral reconstruction using a smaller footprint. Further to this, the laser direct-writing nature of our approach allows seamless integration of our MOD elements with mature laser-inscribed photonic structures such as various optical waveguides[46–48], creating more complex optical dispersion systems. These advantageous characteristics are anticipated to inspire more studies in the future.

In summary, our work represents a breakthrough in achieving microscale optical modulation in high-refractive-index dielectric environments and ultra-broadband optical dispersion with multi-degree-of-freedom controllability. The proposed fabrication method, dispersion mechanism, and manipulation principles provide a versatile and accessible platform thatunlocks new opportunities for enhancing light-matter interactionsin a wide range of transparent dielectric materials andfor advancing free-space integrated spectroscopic devices and systems. These advancements offer a substantial step forward in widely applying optically dispersive components for next-generation portable, wearable, and modular optoelectronic systems, from 2D on-chip to 3D in-chip configurations.

Methods

Materials

In this study, all the crystals used as the matrix for generating MOD are commercially available, and these bulk crystals are generally sized 10 × 10 × 10 mm Z-cut with all sides polished.

Ultrafast laser processing

The dispersive microregions are produced in $LiNbO_3$ crystals by using a standard ultrafast laser direct lithography system (Supplementary Fig. 1a). The light source applied for creating dispersive microregions is a mode-locked regeneratively amplified Yb: KGW-based ultrafast laser

https://doi.org/10.1038/s41467-025-61317-9

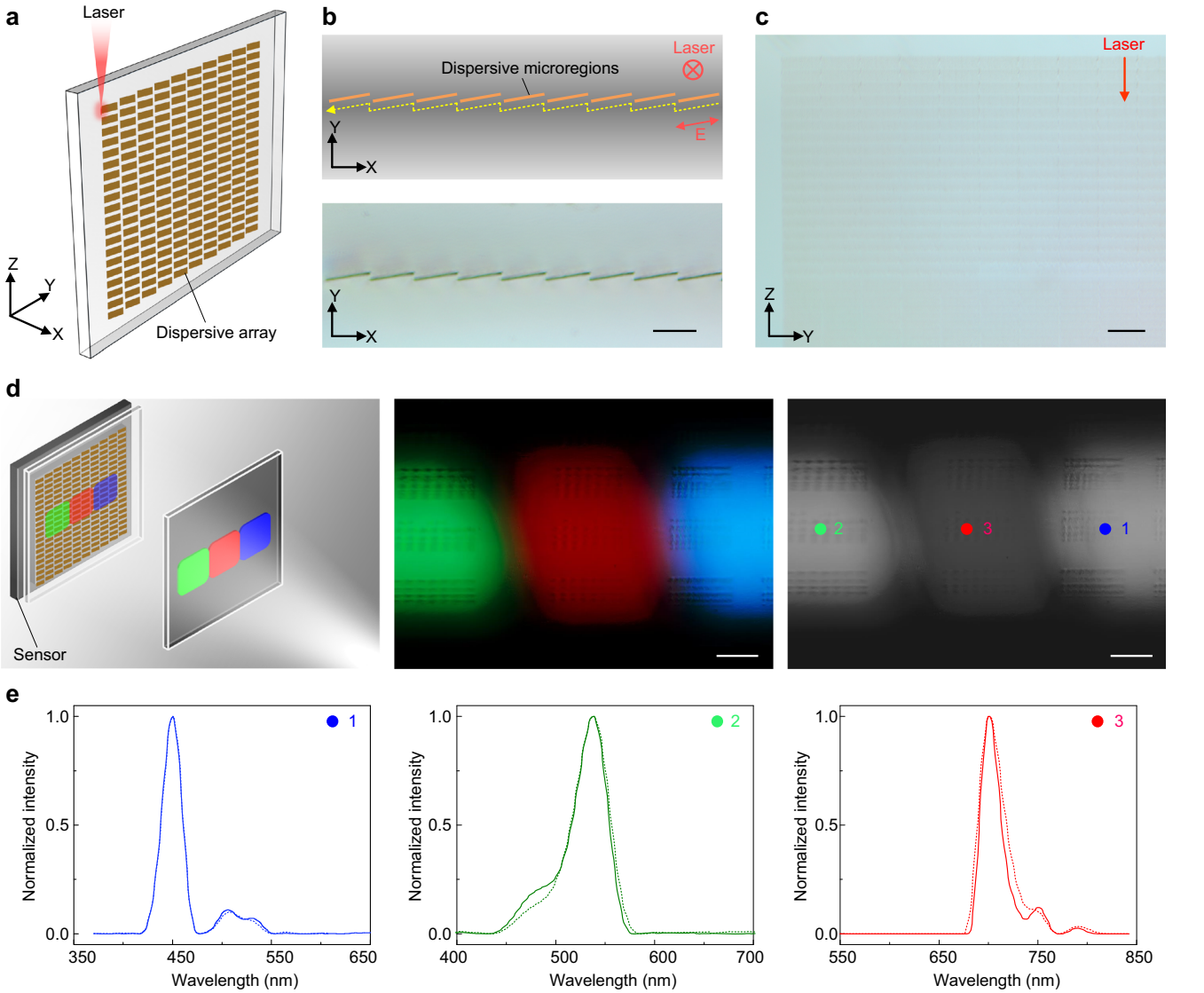

Fig. 5 | Spectral imaging through MOD. a Schematic of dispersive array embedded in a $LiNbO_3$ window. **b** Zigzag laser scanning strategy (dashed line) for fabricating the dispersive array (up) and experimental results (down). E indicates the laser polarization. **c** Optical microscope image of a fabricated dispersive array. **d** Schematic of spectral imaging using MOD spectrometer with a dispersive array (left), normal RGB image of a color filter (middle), and MOD image captured by our spectrometer (right). **e** Reconstructed spectra (solid lines) and reference spectra measured by a commercial spectrometer (dashed lines) at points 1, 2, 3 marked in **d** (right). Scale bars: 100 μm.

(PHAROS, Light Conversion Ltd.) with a wavelength of 1030 nm, a pulse duration ranging from 230 fs to 6 ps, and a pulse repetition rate ranging from 1 to 200 kHz. During the fabrication process, laser parameters such as pulse energy, pulse duration, polarization, and repetition rate are controlled by a computer, and the 3D movement of the sample is controlled using a translation stage. The parameters for inducing SPNs in $LiNbO_3$, as well as in other crystals as shown in Fig. 3f are similar. Generally, to directly induce SPNs in various crystals, an ultrafast laser is tightly focused inside the sample via a 50× objective lens (NA = 0.8). The laser operates with a pulse duration of 1-2 ps (generally 1 ps for all crystals), a repetition rate of 50–200 kHz, a typical writing depth of 60–180 μm, pulse energy of 0.5-2 μJ ($LiNbO_3$: 0.5-2 μJ; $LiTaO_3$: 1.2 μJ; YVO_4: 1 μJ; TiO_2: 1.3 μJ), and a scanning speed of 50–200 μm s^{-1} (generally 80 μm s^{-1} for all crystals). The optimal relative angle between the laser polarization direction and scanning direction is 0° (Supplementary Fig. 19). A standard chromatic polarization microscopy system with a confocal spectrometer is employed to characterize the MOD signals in dispersive microregions (Supplementary Fig. 1b). To precisely control the wedge angle, the $LiNbO_3$ sample needs to be precisely cut and polished to ensure that it is a standard rectangular parallelepiped. The sample is precisely positioned and fixed on a computer-controlled three-dimensional high-precision translation stage, ensuring that one of its edges is parallel to a motion axis of the translation stage. The movement of this translation stage is governed by a computer program, enabling automated control of the ultrafast laser writing path. Taking a vertex of the sample as a reference, the three-dimensional spatial coordinates of the laser scanning path can be calculated according to the desired wedge angle. Inputting these spatial coordinates into the computer, dispersive microregions with a specified wedge angle are fabricated through the movement of the high-precision translation stage during ultrafast laser processing.

Structural characterization

The optical observation of dispersive microregions was performed using a microscope (BX53 Olympus). The inner structure of dispersive microregions was examined by scanning electron microscopy (SEM), using backscattering mode (Gemini300 Zeiss). For the SEM

observation, samples were polished so as to expose SPNs to air and the polished surface was etched with hydrofluoric acid (5%) to improve the contrast of SEM images. Further characterization of the crystal-to-glass phase transition zone of SPNs was performed by focused ion beam (FIB) slicing and high-resolution transmission electron microscopy.

Stability characterization

For heat resistance, the heating rate is 8 °C min^{-1}, with the MOD element maintained in a muffle furnace for 6 h at a temperature of 600 °C. The resistance of the MOD element to contaminants is tested by immersing the sample in high refractive index (~1.5) oil. As the dispersive microregions are embedded inside the crystal matrix, our MOD elements support the direct removal of any contamination on the surface without causing any damage to their delicate photonic structures. For mechanical damage, a sharp object such as a steel needle, serving as an impactor, is used to apply a rapid impact force and scratch the crystal, producing mechanical damage such as fractures and scratches on the surface. The resistance to light damage is tested by continuously irradiating the sample with intense ultraviolet light (405 nm, 100 kW cm^{-2}) for 10 h. We assess the stability of the MOD based on the accurate and reproducible extraction of the spectral characteristics in the MOD region before and after the stability test (Supplementary Fig. 20).

Spectrometer performance measurement

The performance of the MOD-based spectrometer is measured by the spectral analysis system (Supplementary Fig. 1c). In practice, the MOD element is always integrated with a polarizer to ensure the whole device operates under optimal conditions. When analyzing unpolarized natural light, to obtain the highest interference fringe contrast, the intensity of O and E light beams should be balanced (light intensity ratio is 1:1), which can be easily achieved by setting the orientation of the polarizing film coated on the crystal surface (the first polarizer) to precisely fix the input polarization direction at a 45° angle relative to the crystal's optical axis. It is worth noting that when the incident light is linearly polarized, there is a possibility that the incident light is extinct (i.e., the incident polarization is perpendicular to the first polarizer), inhibiting the generation of MOD signals. When this happens, the spectral information can still be detected by slightly rotating the device to avoid the most unfavorable position.

The tunable light source for calibrating the spectrometer is dispersed from a xenon lamp with an adjustable wavelength range from 350 to 1750 nm. The FWHM of monochromatic light is approximately ~3 nm, the power of which is adjusted by an attenuator (LBTEK). The wavelength and power of incident light are collected by commercial spectrometers (USB2000 + , NIRQuest+ Ocean Optics) and a power meter, respectively. The incident light is homogenized by a diffuser and then is modulated by two polarizers as well as fabricated samples to create MOD signals. The intensity distribution of dispersion signals can be read out from an image sensor. The polarizers, sample, and image sensor can be integrated together as a spectroscopic chip.

Data availability

All data needed to support the conclusions in the paper are available in the main text or the supplementary materials.

References

1. Hu, Y. et al. Asymptotic dispersion engineering for ultra-broadband meta-optics. *Nat. Commun.* **14**, 6649 (2023).
2. Picqué, N. & Hänsch, T. W. Frequency comb spectroscopy. *Nat. Photonics* **13**, 146–157 (2019).
3. Del'Haye, P., Arcizet, O., Gorodetsky, M. L., Holzwarth, R. & Kippenberg, T. J. Frequency comb assisted diode laser spectroscopy for measurement of microcavity dispersion. *Nat. Photonics* **3**, 529–533 (2009).
4. Łaszczych, Z. & Soboń, G. Dispersion management of a nonlinear amplifying loop mirror-based erbium-doped fiber laser. *Opt. Express* **29**, 2690–2702 (2021).
5. Chen, W. T., Zhu, A. Y. & Capasso, F. Flat optics with dispersion-engineered metasurfaces. *Nat. Rev. Mater.* **5**, 604–620 (2020).
6. Wise, F. W., Chong, A. & Renninger, W. H. High-energy femtosecond fiber lasers based on pulse propagation at normal dispersion. *Laser Photonics Rev.* **2**, 58–73 (2008).
7. Wang, X. et al. Advances in information processing and biological imaging using flat optics. *Nat. Rev. Electr. Eng.*, **1**, 391–411 (2024).
8. Goda, K. & Jalali, B. Dispersive Fourier transformation for fast continuous single-shot measurements. *Nat. Photonics* **7**, 102–112 (2013).
9. Sun, H., Zhou, Y. & Li, L. Miniature integrated spectrometers towards high-performance and cost-effective. *Light. Sci. Appl.* **12**, 259 (2023).
10. Yang, Z., Albrow-Owen, T., Cai, W. & Hasan, T. Miniaturization of optical spectrometers. *Science* **371**, eabe0722 (2021).
11. Bacon, C. P., Mattley, Y. & DeFrece, R. Miniature spectroscopic instrumentation: applications to biology and chemistry. *Rev. Sci. Instrum.* **75**, 1–16 (2004).
12. Pohl, D. et al. An integrated broadband spectrometer on thin-film lithium niobate. *Nat. Photonics* **14**, 24–29 (2020).
13. Wang, Z. et al. Single-shot on-chip spectral sensors based on photonic crystal slabs. *Nat. Commun.* **10**, 1020 (2019).
14. Gao, B., Shi, Z. & Boyd, R. W. Design of flat-band superprism structures for on-chip spectroscopy. *Opt. Express* **23**, 6491–6496 (2015).
15. Calafiore, G. et al. Holographic planar lightwave circuit for on-chip spectroscopy. *Light. Sci. Appl.* **3**, e203 (2014).
16. Redding, B., Fatt Liew, S., Bromberg, Y., Sarma, R. & Cao, H. Evanescently coupled multimode spiral spectrometer. *Optica* **3**, 956–962 (2016).
17. Bao, J. & Bawendi, M. G. A colloidal quantum dot spectrometer. *Nature* **523**, 67–70 (2015).
18. Monakhova, K., Yanny, K., Aggarwal, N. & Waller, L. Spectral DiffuserCam: lensless snapshot hyperspectral imaging with a spectral filter array. *Optica* **7**, 1298–1307 (2020).
19. Yang, Z. et al. Single-nanowire spectrometers. *Science* **365**, 1017–1020 (2019).
20. Yoon, H. H. et al. Miniaturized spectrometers with a tunable van der Waals junction. *Science* **378**, 296–299 (2022).
21. Faraji-Dana, M. et al. Compact folded metasurface spectrometer. *Nat. Commun.* **9**, 4196 (2018).
22. McClung, A., Mansouree, M. & Arbabi, A. At-will chromatic dispersion by prescribing light trajectories with cascaded metasurfaces. *Light. Sci. Appl.* **9**, 93 (2020).
23. Wang, Z. et al. 3D imprinting of voxel-level structural colors in lithium niobate crystal. *Adv. Mater.* **35**, 2303256 (2023).
24. Hackett, L. et al. Giant electron-mediated phononic nonlinearity in semiconductor–piezoelectric heterostructures. *Nat. Mater.* **23**, 1386–1393 (2024).
25. Guo, Q. et al. Ultrafast mode-locked laser in nanophotonic lithium niobate. *Science* **382**, 708–713 (2023).
26. Yu, M. et al. Integrated femtosecond pulse generator on thin-film lithium niobate. *Nature* **612**, 252–258 (2022).
27. Guo, Q. et al. Femtojoule femtosecond all-optical switching in lithium niobate nanophotonics. *Nat. Photonics* **16**, 625–631 (2022).
28. Li, L., Kong, W. & Chen, F. Femtosecond laser-inscribed optical waveguides in dielectric crystals: a concise review and recent advances. *Adv. Photonics* **4**, 024002–024002 (2022).
29. Wu, B., Zhang, B., Wang, L. & Chen, F. 3D polarization-dependent waveguide arrays in LiNbO 3 crystal produced by femtosecond laser writing. *J. Lightwave Technol.* **38**, 3988–3993 (2020).
30. Thomson, R. R., Campbell, S., Blewett, I. J., Kar, A. K. & Reid, D. T. Optical waveguide fabrication in z-cut lithium niobate (LiNbO3)

using femtosecond pulses in the low repetition rate regime. *Appl. Phys. Lett.* **88**, 111109 (2006).
31. Wei, D. et al. Experimental demonstration of a three-dimensional lithium niobate nonlinear photonic crystal. *Nat. Photonics* **12**, 596–600 (2018).
32. Wei, D. et al. Efficient nonlinear beam shaping in three-dimensional lithium niobate nonlinear photonic crystals. *Nat. Commun.* **10**, 4193 (2019).
33. Deng, W. et al. Electrically tunable two-dimensional heterojunctions for miniaturized near-infrared spectrometers. *Nat. Commun.* **13**, 4627 (2022).
34. Imbrock, J., Hanafi, H., Ayoub, M. & Denz, C. Local domain inversion in MgO-doped lithium niobate by pyroelectric field-assisted femtosecond laser lithography. *Appl. Phys. Lett.* **113**, 252901 (2018).
35. Zhang, B., Liu, X. & Qiu, J. Single femtosecond laser beam induced nanogratings in transparent media-Mechanisms and applications. *J. Mater.* **5**, 1–14 (2019).
36. Yao, H., Pugliese, D., Lancry, M. & Dai, Y. Ultrafast laser direct writing nanogratings and their engineering in transparent materials. *Laser Photonics Rev.* **18**, 2300891 (2024).
37. Karpinski, P., Shvedov, V., Krolikowski, W. & Hnatovsky, C. Laser-writing inside uniaxially birefringent crystals: fine morphology of ultrashort pulse-induced changes in lithium niobate. *Opt. Express* **24**, 7456–7476 (2016).
38. Shur, V. Y. et al. In situ investigation of formation of self-assembled nanodomain structure in lithium niobate after pulse laser irradiation. *Appl. Phys. Lett.* **99**, 082901 (2011).
39. Özer, N. & Lampert, C. M. Electrochemical lithium insertion in sol-gel deposited LiNbO3 films. *Sol. Energy Mater. Sol. Cells* **39**, 367–375 (1995).
40. Choy, T. C. *Effective medium theory: principles and applications*. Oxford University Press (2015).
41. Zhang, B., Wang, Z., Tan, D. & Qiu, J. Ultrafast laser-induced self-organized nanostructuring in transparent dielectrics: fundamentals and applications. *PhotoniX* **4**, 24 (2023).
42. Lei, Y. et al. Ultrafast laser writing in different types of silica glass. *Laser Photonics Rev.* **17**, 2200978 (2023).
43. Zhang, M., Lin, G., Dong, C. & Wen, L. Amorphous TiO2 films with high refractive index deposited by pulsed bias arc ion plating. *Surf. Coat. Technol.* **201**, 7252–7258 (2007).
44. Bian, L. et al. A broadband hyperspectral image sensor with high spatio-temporal resolution. *Nature* **635**, 73–81 (2024).
45. Hamamatsu mini-spectrometer micro series C12666MA. https://www.hamamatsu.com/jp/en/product/optical-sensors/spectrometers/mini-spectrometer/C12666MA.html.
46. Piromjitpong, T. Femtosecond laser inscription of optical waveguide-based devices on lithium niobate.). Aston University (2020).
47. Chakrabarti, M. Refractive index modification in LiNbO3 using femtosecond laser waveguide inscription for integrated optics.). Heriot-Watt University (2008).
48. Jaque, D. et al. Ultrafast laser inscription of bistable and reversible waveguides in strontium barium niobate crystals. *Appl. Phys. Lett.* **96**, 191104 (2010).

Acknowledgements

This work was financially supported by the National Natural Science Foundation of China (grant Nos. 52432001 (J.Q.), 12304349 (B.Z.), U20A20211 (J.Q.), 62275233 (D.T.), 62104212 (Z.Y.), 62334001 (Z.Y.)), the National Key R&D Program of China (grants Nos. 2021YFB2802001 (J.Q.), 2023YFB3405600 (Z.Y.), 2022YFB3206001 (Z.Y.)), the Postdoctoral Fellowship Program of CPSF (grant Nos. GZB20230628 (B.Z.), GZC20241465 (Z.W.)), "Pioneer" and "Leading Goose" R&D Program of Zhejiang (2023C03089 (J.Q.)), the leading innovation and entrepreneurship team project in Zhejiang (2022R01001 (Z.Y.)), and funding from a Leverhulme Trust Early Career Fellowship grant, reference ECF-2022-711 (T.A.-O.).

Author contributions

B.Z., Z.W., and T.A.-O. contributed equally to this work. B.Z. and Z.W. conceived the idea. B.Z., Z.Y., and J.Q. organized, coordinated, and supervised the project. Z.W., B.Z., and G.Z. performed the experiments and collected the data. Z.W., B.Z., T.A.-O., Z.Y., and J.Q. interpreted the results and proposed the mechanism. Z.W., B.Z., T.A.-O., D.T., and Z.Y. wrote the manuscript. T.H., Z.C., Z.S., H.J., Q.G. and C.Q., supervised and reviewed the manuscript. Z.W., B.Z., D.T., Z.Y., and J.Q. discussed and revised the manuscript.

Competing interests

The authors declare no competing interests.

Additional information

Supplementary information The online version contains supplementary material available at https://doi.org/10.1038/s41467-025-61317-9.

Correspondence and requests for materials should be addressed to Bo Zhang, Dezhi Tan, Cheng-wei Qiu, Zongyin Yang or Jianrong Qiu.

Peer review information *Nature Communications* thanks the anonymous reviewer(s) for their contribution to the peer review of this work. A peer review file is available.